Structure–Function Analysis of Friedreich's Ataxia Mutants Reveals Determinants of Frataxin Binding and Activation of the Fe–S Assembly Complex

Jennifer Bridwell-Rabb, **Andrew M. Winn**, and **David P. Barondeau**[*]
Department of Chemistry, Texas A&M University, College Station, Texas 77842, United States

Abstract

Friedreich's ataxia (FRDA) is a progressive neurodegenerative disease associated with the loss of function of the protein frataxin (FXN) that results from low FXN levels due to a GAA triplet repeat expansion or, occasionally, from missense mutations in the *FXN* gene. Here biochemical and structural properties of FXN variants, including three FRDA missense mutations (N146K, Q148R, and R165C) and three related mutants (N146A, Q148G, and Q153A), were determined in an effort to understand the structural basis for the loss of function. In vitro assays revealed that although the three FRDA missense mutations exhibited similar losses of cysteine desulfurase and Fe–S cluster assembly activities, the causes for these activation defects were distinct. The R165C variant exhibited a k_{cat}/K_M higher than that of native FXN but weak binding to the NFS1, ISD11, and ISCU2 (SDU) complex, whereas the Q148R variant exhibited the lowest k_{cat}/K_M of the six tested FXN variants and only a modest binding deficiency. The order of the FXN binding affinities for the SDU Fe–S assembly complex was as follows: FXN > Q148R > N146A > Q148G > N146K > Q153A > R165C. Four different classes of FXN variants were identified on the basis of their biochemical properties. Together, these structure–function studies reveal determinants for the binding and allosteric activation of the Fe–S assembly complex and provide insight into how FRDA missense mutations are functionally compromised.

Friedreich's ataxia (FRDA) is a currently incurable autosomal recessive neurodegenerative disease caused by reduced amounts of the protein frataxin (FXN).[1] The majority (>95%) of FRDA patients are homozygous for an unstable GAA trinucleotide repeat expansion in the first intron of the *FXN* gene.[2] The number of repeats ranges from 7 to 40 for normal individuals and from 66 to >1700 for FRDA patients,[2,3] with larger numbers of GAA repeats correlating with lower levels of FXN expression and an earlier age of disease onset.[4,5] A small fraction of FRDA patients are compound heterozygotes with an expanded GAA repeat affecting one allele and a missense or nonsense mutation affecting the other

[*]**Corresponding Author** Department of Chemistry, Texas A&M University, College Station, TX 77842. Telephone: (979) 458-0735. Fax: (979) 458-0736. barondeau@tamu.edu. .

allele.[6] The loss of FXN results in a complex phenotype that includes an increased level of iron in the mitochondria, deficiencies in Fe–S cluster enzymes, and enhanced sensitivity to oxidative stress.[7] The diminished in vivo activity for Fe–S proteins suggests that FXN may have a role in iron–sulfur (Fe–S) cluster assembly.[8,9]

Human Fe–S cluster biosynthesis occurs in the matrix space of the mitochondria and is catalyzed by a four-component core complex composed of NFS1, ISD11, ISCU2, and FXN,[10,11] which is also known as the SDUF complex. The cysteine desulfurase NFS1, which forms a functional complex with ISD11,[12–14] catalyzes the PLP-dependent breakdown of cysteine to alanine and produces a transient persulfide species.[15,16] The terminal sulfur of this species is transferred to the scaffold protein ISCU2 to build [2Fe-2S] and, possibly, [4Fe-4S] cluster intermediates.[17,18] Chaperones interact with the scaffold protein and assist in delivering intact Fe–S clusters to their apo targets.[19–21] Many functions have been proposed for frataxin[22] in Fe–S cluster biosynthesis, including a role as an iron chaperone[23,24] and a role, either positive[11] or negative,[25] in regulating cluster assembly.

Molecular level details are lacking for protein–protein interactions between human FXN and the other components of the SDUF Fe–S assembly complex. Recently, a crystal structure was determined for a protein complex between the cysteine desulfurase IscS and scaffold protein IscU for a prokaryotic system,[26] and SAXS data suggest a potential binding site for the FXN homologue CyaY on this IscS–IscU complex.[26,27] The structures of human NFS1, ISD11, and ISCU2 have not been determined. The FXN structure (Figure 1A) has N- and C-terminal α-helices that pack against an antiparallel β-sheet.[28-30] NMR studies of the *Saccharomyces cerevisiae* FXN homologue Yfh1[31] along with pull-down studies for frataxin variants[10,32-34] indicate residues on the β-sheet such as V144, N146, Q148, Q153, W155, and R165 (human numbering) contribute to binding interactions between FXN and other Fe–S assembly proteins. Interestingly, many of these residues are also identified as FRDA missense mutations, including the N146K, Q148R, W155R, and R165C variants.[2] Previous structure–function studies of FXN variants led to a model in which residue W155 undergoes a conformational change to occupy a surface cavity, similar to the position of residue 155 in the W155R and W155F structures (Figure 1B), to interact with and activate the SDU complex for sulfur transfer and Fe–S cluster biosynthesis.[35]

Here FRDA clinical variants N146K, Q148R, and R165C, along with related N146A, Q148G, and Q153A variants, were constructed for the evaluation of the FXN binding model[35] and also the examination of how FRDA missense variants are functionally compromised. The determination of binding constants, functional properties in cysteine desulfurase and Fe–S cluster assembly assays, and crystal structures of five of the variants reveals structure–function correlations and details for how these residues contribute to binding and allosteric activation[11] of the human Fe–S assembly complex.

EXPERIMENTAL PROCEDURES

Protein Preparation

The QuikChange method (Strata-gene) was used to introduce point mutants (N146A, N146K, Q148G, Q148R, Q153A, and R165C) into a pET11a plasmid containing a codon-optimized human *FXN* gene lacking the first 55 amino acids (FXN Δ1–55),[11] and the mutant genes were confirmed by DNA sequencing. The plasmids containing mutant *FXN* genes were individually transformed into *Escherichia coli* strain BL21(DE3) cells and grown at 37 °C. When the cells reached an OD_{600} of ~0.6, the temperature was reduced to 16 °C and protein expression was induced with 0.5 mM isopropyl β-D-1-thiogalactopyranoside (IPTG). Cells were harvested 16 h later and lysed by sonication (Branson Sonifier 450) in 50 mM Tris (pH 7.5). The supernatant was loaded onto an anion exchange column (26/20

POROS 50HQ, Applied Biosystems) and eluted with a linear gradient from 0 to 800 mM NaCl in 50 mM Tris (pH 7.5). FXN-containing fractions were collected and further purified on a Sephacryl S100 (26/60, GE Healthcare) size-exclusion column equilibrated in 50 mM HEPES (pH 7.5) and 150 mM NaCl. ISCU2 and the NFS1–ISD11 complex were purified as previously described.[11] Protein concentrations for the FXN variants were estimated by their absorbance at 280 nm using an extinction coefficient of 26030 M^{-1} cm^{-1}.[36] Protein concentrations for the NFS1–ISD11 complex and ISCU2 were estimated using extinction coefficients of 42670 and 8250 M^{-1} cm^{-1},[36] respectively.

Cysteine Desulfurase Activity Measurements

Reactions were performed as previously described in a total volume of 800 μL.[11,37,38] Briefly, reaction mixtures containing 0.5 μM NFS1–ISD11 complex (SD), 1.5 μM ISCU2, and 1.5 μM FXN (or FXN point mutant) were incubated with 10 μM pyridoxal 5′-phosphate (PLP), 2 mM dithiothreitol (DTT), 5 μM Fe(NH$_4$)$_2$(SO$_4$)$_2$, 50 mM Tris (pH 8.0), and 250 mM NaCl for 30 min in an anaerobic (10–14 °C) glovebox.[11] The cysteine desulfurase reaction was initiated with 100 μM L-cysteine at 37 °C and quenched by the addition of 100 μL of 20 mM N,N-dimethyl-p-phenylenediamine in 7.2 N HCl and 100 μL of 30 mM FeCl$_3$ in 1.2 N HCl. Methylene blue formation was measured at 670 nm after a 20 min incubation of the quenched reaction mixtures at 37 °C and compared to a Na$_2$S standard curve to quantitate sulfide production. Units are defined as micromoles of sulfide per micromole of SD per minute at 37 °C. The rates for the cysteine desulfurase reaction were also examined with increasing amounts of FXN (or FXN variant) to determine the number of equivalents, or the saturating amount, required to maximize the cysteine desulfurase activity.

Fe–S Cluster Formation

Fe–S cluster biosynthetic assays were performed as previously described in a total volume of 200 μL.[11] Assay mixtures containing 24 μM ISCU2 were incubated with 5 mM DTT in 50 mM Tris (pH 8.0) and 250 mM NaCl in an anaerobic glovebox for 1 h prior to addition of 8 μM SD, 24 μM FXN (or FXN variants), and 200 μM Fe(NH$_4$)$_2$(SO$_4$)$_2$. The reaction was initiated at room temperature with 100 μM cysteine injected from a gastight syringe and monitored at 456 nm. The time-dependent increase in absorbance at 456 nm was fit over the first 1000 s to first-order kinetics using KaleidaGraph (Synergy Software), and the rate was converted to the amount of [2Fe-2S] cluster formed using an extinction coefficient of 9.8 mM^{-1} cm^{-1}.[39] Units are defined as the micromoles of [2Fe-2S] cluster formed per micromole of SDU complex per minute at 25 °C.

Michaelis–Menten Kinetics for Frataxin Variants in the SDUF Complex

The saturating amounts of the different FXN variants were added to a standard reaction mixture [0.5 μM SD, 1.5 μM ISCU2, 10 μM PLP, 2 mM DTT, 5 μM Fe(NH$_4$)$_2$(SO$_4$)$_2$, 50 mM Tris (pH 8.0), and 250 mM NaCl] and incubated for 30 min in an anaerobic glovebox. Cysteine desulfurase activity measurements were initiated with the addition of L-cysteine (from 0.01 to 1 mM), and the rates were fit to the Michaelis–Menten equation using Kaleida-Graph. Binding constants were determined for each of the variants by plotting k_{cat} as a function of FXN concentration. The resulting data were fit as a type II allosteric activator[40] to eq 1 using KaleidaGraph.

$$k_{cat} = \frac{k_{SDU} + \frac{k_{SDUF}^{\infty}[Fxn]}{K_d}}{1 + \frac{[Fxn]}{K_d}} \qquad (1)$$

where K_d is the binding constant, k_{SDU} is the k_{cat} in the absence of FXN (0.89 min^{-1}), and k_{SDUF}^{∞} is the k_{cat} with saturated amounts of FXN for the particular variant (Table 1).

Protein Crystallization, Data Collection, and Refinement

Protein crystallization trials for FXN variants at 10 mg/mL in 50 mM Tris (pH 7.5) were initiated with hanging-drop vapor diffusion methods by mixing 2 μL of protein and 2 μL of reservoir solution, followed by incubation at 22 °C. The N146K variant crystallized in 28% PEG monomethyl ether 2000 and 100 mM Tris (pH 7.0). Initial crystallization conditions for the Q148G and R165C variants included 2.0 M ammonium sulfate and 0.1 M sodium citrate (pH 5.5). These initial crystals were used for microseeding with the same reservoir solution except the ammonium sulfate concentration was decreased to 1.9 M. Q148R crystallized in 20% PEG 3000 with 0.1 M sodium citrate (pH 5.5). Q153A crystallized in 2.0 M ammonium sulfate, 0.1 M sodium citrate tribasic dihydrate (pH 5.6), and 0.2 M potassium sodium tartrate tetrahydrate. Single crystals for the N146K, Q148G, Q148R, and Q153A variants were transferred to a cryoprotection solution that contained their respective reservoir solutions and 20% ethylene glycol for ~0.5 min and flash-frozen in liquid nitrogen. The same procedure was used for crystals of the R165C variant except 20% glycerol was substituted for the ethylene glycol. X-ray diffraction data were collected at SSRL beamline 7-1 (ADSC Quantum-315R CCD detector) for crystals of the Q148R and Q153A variants, SSRL beamline 11-1 (MAR 325 CCD detector) for a Q148G crystal, APS beamline 23-ID-D (MAR 300 CCD detector) for an N146K crystal, and ALS beamline 4.2.2 (NOIR-1 CCD detector) for an R165C crystal. The images were integrated and scaled with iMosflm[41] and Scala of the CCP4 suite.[42] Phases for the variants were determined by molecular replacement using Phaser[43] with a previously refined structure of FXN[29] as a search model [Protein Data Bank (PDB) entry 1EKG]. Difference electron density and omit maps were manually fit with XtalView[44] and refined in Refmac5[45] with all of the data except the 5% used for R_{free} calculations.[46] PDB entries are as follows: 3T3J for N146K, 3T3T for Q148G, 3T3K for Q148R, 3T3L for Q153A, and 3T3X for R165C.

RESULTS

Diminished Activity of the Fe–S Assembly Complex Substituted with Frataxin Variants

The N146K, Q148R, and R165C FRDA mutants and related N146A, Q148G, and Q153A FXN variants were heterologously expressed in *E. coli* and purified to >95% homogeneity. These FXN Δ1–55 variants spontaneously truncated N-terminal residues 56–81[47] to generate the mature form of FXN [residues 82–210 (Figure 1 of the Supporting Information)] and exhibited monomeric behavior on size-exclusion chromatography (data not shown). The six variants were tested for their ability to stimulate cysteine desulfurase and Fe–S cluster assembly activities of the reconstituted Fe–S assembly complex composed of NFS1, ISD11, and ISCU2 (SDU). Equivalent amounts of the FXN variants were included in these assays to estimate the in vivo functional consequences of the point mutants (assuming similar protein levels), whereas 100 μM L-cysteine was used to mimic cellular substrate concentrations.[11] All six FXN variants exhibited decreased activity compared to that of native FXN (Figure 2) in the following order: FXN > N146A > Q148G > Q148R ~ R165C ~ N146K > Q153A > SDU (Table 1). These activities are significantly higher than those from previous control assays with 100 μM sulfide rather than cysteine,[35] which indicated that efficient Fe–S cluster formation was not mediated by sulfide in solution. Notably, the relative activities of FRDA variants N146K, Q148R, and R165C were similar in the cysteine desulfurase and Fe–S cluster assembly assays.

Binding Affinity of Frataxin Variants for the SDU Complex

Next, binding constants for the variants were determined to explore if the lower activation levels were due to weaker binding of the FXN variants to the SDU complex. The rates of sulfide production were determined as a function of L-cysteine concentration at different concentrations of added FXN, as previously described for the I154F and W155 variants.[35] The resulting k_{cat} values were plotted against the FXN concentration, and the data were fit as a type II allosteric activator to eq 1 (Figure 3). Previously, a K_d of 0.22 μM was determined for native FXN binding to the SDU complex.[35] Here binding constants range from 0.85 to 10.40 μM for the six FXN variants (Table 1). The weaker binding for N146K compared to that of N146A is consistent with previous pull-down experiments.[10] Interestingly, the Q148R and R165C variants, which have similar ability to activate the Fe–S assembly complex under standard conditions (Figure 2), exhibited the tightest and weakest binding of the six variants, respectively.

Kinetic Parameters for Assembly Complexes Substituted with Frataxin Variants

The Michaelis–Menten kinetic parameters for the cysteine desulfurase reaction were determined for the SDUF complex with the different FXN variants under conditions in which each FXN variant was saturating to compensate for weaker binding. Cysteine desulfurase activity was measured as a function of added FXN variant concentration to determine the amount required to reach saturation for binding of FXN to the SDU complex. The activity was maximized by the addition of 3 equiv of wild-type FXN, 10 equiv of Q148R, 30 equiv of N146A, 50 equiv of Q148G and N146K, 90 equiv of R165C, or 100 equiv of Q153A (data not shown). Saturating amounts of the different FXN variants were then added to the SDU complex, and the rates of the cysteine desulfurase reaction were measured as a function of L-cysteine concentration. The R165C variant, which is the weakest binding of the six variants, exhibited activation of the SDU complex (under saturating FXN conditions) that was equivalent to that of native FXN (Table 1). In contrast, the tightest binding variant, Q148R, exhibited the lowest k_{cat}/K_M, which is lower than that of native FXN by a factor of ~5.

Crystal Structures for Frataxin Variants

High-resolution crystal structures (Table 2) were determined for the N146K, Q148G, Q148R, Q153A, and R165C variants in an effort to understand the structural basis for altered functional properties (Table 1). Previously, residue W155 was shown to contribute to binding interactions with partner proteins and also be important for frataxin function in Fe–S cluster biosynthesis.[10,32,34,35] The orientation of the W155 side chain is constrained by a hydrogen bond between the indole ring nitrogen and the side chain oxygen of Q153, as well as van der Waals interactions with the side chains of N146, Q148, and R165 (Figure 1A). In addition, the N146 side chain nitrogen atom forms a hydrogen bond to the backbone carbonyl of K147; Q148, whose side chain oxygen forms a hydrogen bond to N151, is the first residue in an α-turn between β-strands 3 and 4, and R165 exhibits no intramolecular hydrogen bonds to other FXN residues but is appropriately positioned to form a cation–π interaction with W155.

The N146K FRDA missense mutant crystallized in the $P2_1$ space group; the crystals diffracted to 1.70 Å resolution (Table 2), and the refined structure exhibited backbone (Cα rmsd = 0.30 Å) and side chain conformations similar to those of native FXN. In the N146K structure (Figure 4A), the W155 side chain stacked between the Q148 and R165 side chains, similar to native FXN, and exhibited a hydrogen bond pattern similar to that of FXN (Figure 4B). Changes due to the N146K mutation include the loss of a hydrogen bond between the side chain of residue 146 and the carbonyl oxygen of K147 and localized alteration in the electrostatic and molecular surface of FXN.

The Q148R FRDA missense mutation crystallized in the $P2_12_12_1$ space group (Table 2), and the 1.24 Å electron density maps (Figure 4C) revealed very minor structural rearrangements relative to native FXN ($C\alpha$ rmsd = 0.44 Å). The positions of W155, R165, and the backbone conformation of the α-turn initiated by residue 148 were not altered by the Q148R substitution (Figure 4D). The electron density revealed that the Q148R substitution, which provided part of the pocket for W155 in the native FXN structure (Figure 1A), was in position to provide cation–π stabilization for the W155 side chain. In addition, residue N151 rearranged to form a hydrogen bond with the Q153, rather than Q148, side chain. Although the N146K and Q148R variants incorporate a positively charged residue, the structures reveal minor overall changes to the binding surface of FXN.

The Q148 residue was also mutated to a glycine, and the purified Q148G protein crystallized in the $P2_1$ space group with four molecules in the asymmetric unit (Table 2). The 1.38 Å resolution electron density maps (Figure 4E) revealed a rearrangement of the α-turn (between β-strands 3 and 4) that positioned P150 to pack against a rotated W155 side chain. Overlaying the four independent molecules in the asymmetric unit revealed one conformation for W155, but two conformations for N146 and R165 (Figure 4F). The electron density for two of the four Q148G molecules in the asymmetric unit indicated R165 occupies two alternate side chain conformations, with one of these conformers positioned to hydrogen bond to the N151 and Q153 side chains (Figure 4E). Minor rearrangements were also observed for residues S157 and P163.

The Q153 side chain, which formed a hydrogen bond to W155 in the native FXN structure (Figure 1A), was mutated to an alanine, and the recombinant protein crystallized in the $C2$ space group (Table 2). The 1.15 Å resolution electron density maps (Figure 4G) revealed substantial rearrangements near the mutation site. Residue N151 underwent a conformational change to replace the hydrogen bond to W155 eliminated by the Q153A substitution (Figure 4H). The R165 side chain exhibited two conformations, which would be sterically forbidden in the native FXN structure, to form hydrogen bonds with the backbone carbonyl of N151 and to the side chain of D167. This new position for R165 allowed a rearrangement of the W155 side chain.

The FRDA missense mutation R165C crystallized in the $C2$ space group with two molecules in the asymmetric unit (Table 2). The 1.57 Å resolution electron density maps revealed one molecule was significantly better ordered and was modeled with the R165C side chain in three distinct conformations, the N146 side chain in two conformations, and the W155 indole ring in multiple positions (Figure 4I). Additional electron density near one of the alternate conformations of W155 was due to a symmetry molecule (not shown). A third conformation for the W155 side chain was found in the other molecule in the asymmetric unit that was oriented like that of native FXN (Figure 4J). Together, these crystal structures coupled with kinetic analysis help define the determinants for FXN binding and function as an allosteric activator for the SDU complex.

DISCUSSION

Previously, FXN missense I154F and W155R mutations present in compound heterozygous patients were shown to exhibit binding and activation defects in cysteine desulfurase and Fe–S cluster biosynthesis assays.[35] The magnitude of these defects appeared to correlate with the clinical phenotype and suggested that biochemical characterization of FRDA mutants may provide mechanistic insight and details into how FXN variants are functionally compromised. On the basis of these results, a model was proposed in which FXN residue W155 undergoes a conformational change to fill an empty pocket [between W155 and S157 (see Figure 1A)] on the surface of the protein and position W155 for binding and activation

of the SDU complex.[35] Here additional FRDA missense mutations N146K, Q148R, and R165C, along with related N146A, Q148G, and Q153A variants, were evaluated to improve our understanding of biochemical defects in FRDA missense mutations and test this initial binding and activation model. Interestingly, the three FRDA missense mutants exhibited similar deficiencies in cysteine desulfurase and Fe–S cluster formation activities (Table 1), but the causes of these activation defects were dramatically different. The R165C variant exhibited a k_{cat}/K_M higher than that of native FXN but weak binding to the SDU complex, whereas the Q148R variant exhibited a much lower k_{cat}/K_M and an only modest binding deficiency. Crystal structures for five of these FXN variants were determined to provide insight into how these mutations result in changes in binding and activation of the SDU complex.

Biochemical data for the FRDA missense and related FXN variants presented here and in a previous paper[35] suggest four general classes of FXN variants, each of which contains FRDA missense mutations. Class I variants (Q153A and W155R) displayed weak binding (at least 25-fold weaker than that of FXN) and substantially reduced cysteine desulfurase activity (k_{cat} less than 30% of that of FXN). Class II variants (R165C, N146K, and W155A) displayed weak binding but possessed a level of catalysis that was only mildly reduced (k_{cat} more than 45% of that of FXN). Class III variants (Q148R) had only modest defects in binding (3–10-fold weaker than that of FXN) but a substantially reduced level of catalysis (k_{cat} less than 25% of that of FXN). Class IV variants (W155F, N146A, Q148G, and I154F) had only modest defects in both binding and activation of the SDU complex.

The crystal structures for the class I and II variants that bound at least 25-fold more weakly to the SDU complex [R165C < Q153A < W155R < N146K < W155A (Figure 5A)] suggested that two factors contributed to the binding defects. First, the weakest binding variant, R165C, lacks the guanidinium group of the R165 side chain; the Q153A variant exhibits two conformations for R165 that are distinct from that of native FXN and are stabilized by hydrogen bond interactions with D167 and N151, and the W155A variant underwent a rearrangement of the R165 side chain to hydrogen bond to Q153 (Figure 5A). In these mutants, the guanidinium group of the R165 side chain is not available or less able to interact with partner proteins. Second, the W155R and N146K structures (Figure 5A) revealed the presence of positively charged residues that are adjacent to a surface pocket near S157 that may lower the binding affinity of FXN for SDU. In contrast, the available crystal structures of the class III and IV variants that bind only 3–10-fold more weakly than the wild type (Q148G < W155F < N146A < Q148R < I154F) revealed that the R165 side chain was positioned like native FXN and that these variants lacked a positively charged residue near the surface pocket (Figure 5B). Together, these structure–function correlations suggest that FXN binding to the SDU complex is stabilized by the native FXN conformation of R165, whereas a positive charge near a surface pocket destabilizes the complex.

Structure–function properties were also examined for the different FXN variants to understand the determinants for stimulating the cysteine desulfurase reaction of the SDU complex. Crystal structures of class I and III variants, which possess substantially reduced level of activation of the cysteine desulfurase reaction [W155R < Q148R < Q153A (Figure 5C)], revealed that these variants may lose the ability of residue 155 to occupy the surface pocket and activate the SDU complex. The W155R variant substitutes the tryptophan with a positively charged residue; the Q148R mutant stabilized W155 in the native conformation through a cation–π interaction, and the Q153A variant stabilized an alternate conformation of the W155 side chain (Figure 5C). The crystal structures of class II and IV variants, which possess an only moderately reduced level of activation, reveal that the relative effects of the variants (W155A < N146K < Q148G < W155F < N146A < I154F < R165C) can be also linked to their effects on W155 and adjacent residues. The class II and IV variants with

weaker activation (k_{cat} between 45 and 50% of that of FXN) include the W155A variant, which lacks the indole ring of residue 155, the N146K variant, which incorporates a positive charge near the proposed W155 interaction site, and Q148G, which stabilizes an alternate conformation for the W155 side chain (Figure 5D). The class II and IV variants with the highest k_{cat} values (W155F and R165C) placed an aromatic ring in the surface cavity (Figure 5E). Together, these data are consistent with a model for efficient catalysis being mediated when W155 occupies a pocket on the surface of FXN for interactions with partner proteins, possibly through π–π or cation–π interactions, that are inhibited by positive charge.

A general correlation was observed for a log–log plot of the binding constants for the different FXN variants (K_d) and the k_{cat} values for the cysteine desulfurase reaction (Figure 6). Such a correlation has been observed for other systems[48-50] and suggests these FXN variants are altering molecular interactions important for binding to the SDU complex that are also important for stimulating the cysteine desulfurase activity. In Figure 6, variants above the line have stronger binding than activation deficiencies, whereas those below the line exhibit stronger activation than binding defects. A binding defect outlier, R165C, has 50-fold weaker binding to the SDU complex yet exhibits a similar k_{cat} compared to that of native FXN. We hypothesize these properties of R165C are due to the loss of the guanidinium group of the R165 side chain, which primarily contributes to binding, and the positioning of W155 in a pocket for interactions with SDU (Figure 5E). An activation defect outlier, Q148R, exhibits a modest decrease in binding affinity but is one of the most compromised variants in its ability to stimulate the cysteine desulfurase activity of the SDU complex. We hypothesize that these properties of Q148R are due to the near native conformation of R165, which contributes to the binding affinity, and the introduced Q148R positive charge, which provides cation–π interactions to lock W155 in the native FXN conformation and inhibit the proposed conformational change that places the indole ring in a surface pocket for interactions with the SDU complex.

The three FRDA missense mutations R165C, N146K, and Q148R investigated here were equally compromised in the in vitro cysteine desulfurase and Fe–S cluster assembly assays. Initially, one might predict that the clinical consequences of these variants would then be similar. However, the situation is more complicated in FRDA patients with missense mutations, as these patients express both a native FXN from a GAA expanded allele and the mutant FXN from the missense allele. These two forms of FXN would compete for binding to the SDU complex in vivo. The 3–5-fold loss of catalytic efficiency observed for many of the FRDA missense mutants (Table 1) is on the order of the 3–5-fold decrease in FXN levels that appears to be sufficient to develop a FRDA phenotype for patients with two GAA repeat alleles.[51-55] Therefore, class III FXN missense mutants such as Q148R that have an ~5-fold decrease in catalytic efficiency but bind relatively well might be expected to be more detrimental than class II missense mutants such as R165C and N146K that bind weakly but have mild, if any, catalytic deficiencies. Consistent with this idea, patients with the class III mutation Q148R exhibit typical FRDA pathogenesis, while patients with class II mutations R165C and N146K have unusually mild disease progression.[2] Notably, the class I mutant W155R, which is characterized by both weak binding and low activity, is classified as an early onset FRDA missense mutant, whereas the class IV missense mutant I154F with modest binding and activation defects has typical disease progression.[2]

In summary, the results presented here allow an initial classification of FRDA and related FXN variants on the basis of their ability to bind to the SDU complex and stimulate the cysteine desulfurase reaction. The biochemical properties for these different classes of FXN variants may help explain the clinical outcomes for FRDA missense mutations that range from early onset to atypically mild.[2] From a mechanistic perspective, it is difficult to

understand how FXN functions as an activator without molecular level structural data for the SDUF complex. Here we start to define the contributions of individual FXN residues in the binding and activation of the SDU complex that may lead to the design of biomimetics that can therapeutically replace FXN function. Future experiments will be aimed at testing and refining this model for FXN-based activation and defining the role of FXN-interacting residues on NFS1 and ISCU2 that are important for sulfur transfer and Fe–S cluster assembly.

Supplementary Material

Refer to Web version on PubMed Central for supplementary material.

Acknowledgments

ABBREVIATIONS

DTT	dithiothreitol
FRDA	Friedreich's ataxia
FXN	frataxin
HEPES	N-(2-hydroxyethyl)piperazine-N'-2-ethanesulfonicacid
IPTG	isopropyl β-D-1-thiogalactopyranoside
PEG	poly-ethylene glycol
PLP	pyridoxal 5′-phosphate
rmsd	root-mean-square deviation
SD	NFS1–ISD11 protein complex
SDU	NFS1–ISD11–ISCU2 protein complex
SDUF	NFS1–ISD1–ISCU2–frataxin protein complex
Tris	tris(hydroxymethyl)-aminomethane

REFERENCES

(1). Campuzano V, Montermini L, Moltè MD, Pianese L, Cossee M, Cavalcanti F, Monros E, Rodius F, Duclos F, Monticelli A, Zara F, Cañizares J, Koutnikova H, Bidichandani SI, Gellera C, Brice A, Trouillas P, De Michele G, Filla A, De Frutos R, Palau F, Patel PI, Di Donato S, Mandel JL, Cocozza S, Koenig M, Pandolfo M. Friedreich's ataxia: Autosomal recessive disease caused by an intronic GAA triplet repeat expansion. Science. 1996; 271:1423–1427. [PubMed: 8596916]

(2). Santos R, Lefevre S, Sliwa D, Seguin A, Camadro J-M, Lesuisse E. Friedreich's Ataxia: Molecular Mechanisms, Redox Considerations and Therapeutic Opportunities. Antioxid. Redox Signaling. 2010; 13:651–690.
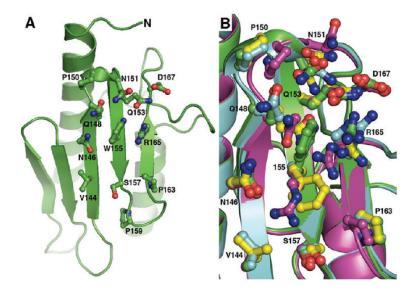
(3). Schöls L, Amoiridis G, Przuntek H, Frank G, Epplen JT, Epplen C. Friedreich's ataxia. Revision of the phenotype according to molecular genetics. Brain. 1997; 120(Part 12):2131–2140. [PubMed: 9448568]

(4). Dürr A, Cossee M, Agid Y, Campuzano V, Mignard C, Penet C, Mandel JL, Brice A, Koenig M. Clinical and genetic abnormalities in patients with Friedreich's ataxia. N. Engl. J. Med. 1996; 335:1169–1175. [PubMed: 8815938]

(5). Filla A, De Michele G, Cavalcanti F, Pianese L, Monticelli A, Campanella G, Cocozza S. The relationship between trinucleotide (GAA) repeat length and clinical features in Friedreich ataxia. Am. J. Hum. Genet. 1996; 59:554–560. [PubMed: 8751856]

(6). Cossee M, Dürr A, Schmitt M, Dahl N, Trouillas P, Allinson P, Kostrzewa M, Nivelon-Chevallier A, Gustavson KH, Kohlschütter A, Müller U, Mandel JL, Brice A, Koenig M, Cavalcanti F, Tammaro A, De Michele G, Filla A, Cocozza S, Labuda M, Montermini L, Poirier J, Pandolfo M. Friedreich's ataxia: Point mutations and clinical presentation of compound heterozygotes. Ann. Neurol. 1999; 45:200–206. [PubMed: 9989622]

(7). Schmucker S, Puccio H. Understanding the molecular mechanisms of Friedreich ataxia to develop therapeutic approaches. Hum. Mol. Genet. 2010; 19:R103–R110. [PubMed: 20413654]

(8). Muhlenhoff U, Richhardt N, Ristow M, Kispal G, Lill R. The yeast frataxin homolog Yfh1p plays a specific role in the maturation of cellular Fe/S proteins. Hum. Mol. Genet. 2002; 11:2025–2036. [PubMed: 12165564]

(9). Stehling O, Elsässer H, Brückel B, Muhlenhoff U, Lill R. Iron-sulfur protein maturation in human cells: Evidence for a function of frataxin. Hum. Mol. Genet. 2004; 13:3007–3015. [PubMed: 15509595]

(10). Schmucker S, Martelli A, Colin F, Page A, Wattenhofer-Donzé M, Reutenauer L, Puccio H. Mammalian Frataxin: An Essential Function for Cellular Viability through an Interaction with a Preformed ISCU/NFS1/ISD11 Iron-Sulfur Assembly Complex. PLoS One. 2011; 6:e16199. [PubMed: 21298097]

(11). Tsai CL, Barondeau DP. Human frataxin is an allosteric switch that activates the Fe-S cluster biosynthetic complex. Biochemistry. 2010; 49:9132–9139. [PubMed: 20873749]

(12). Adam AC, Bornhövd C, Prokisch H, Neupert W, Hell K. The Nfs1 interacting protein Isd11 has an essential role in Fe/S cluster biogenesis in mitochondria. EMBO J. 2006; 25:174–183. [PubMed: 16341090]

(13). Shi Y, Ghosh M, Tong W-H, Rouault TA. Human ISD11 is essential for both iron-sulfur cluster assembly and maintenance of normal cellular iron homeostasis. Hum. Mol. Genet. 2009; 18:3014–3025. [PubMed: 19454487]

(14). Wiedemann N, Urzica E, Guiard B, Müller H, Lohaus C, Meyer HE, Ryan MT, Meisinger C, Muhlenhoff U, Lill R, Pfanner N. Essential role of Isd11 in mitochondrial iron-sulfur cluster synthesis on Isu scaffold proteins. EMBO J. 2006; 25:184–195. [PubMed: 16341089]

(15). Zheng L, White RH, Cash VL, Jack RF, Dean DR. Cysteine desulfurase activity indicates a role for NIFS in metallocluster biosynthesis. Proc. Natl. Acad. Sci. U.S.A. 1993; 90:2754–2758. [PubMed: 8464885]

(16). Johnson DC, Dean DR, Smith AD, Johnson M. Structure, function, and formation of biological iron-sulfur clusters. Annu. Rev. Biochem. 2005; 74:247–281. [PubMed: 15952888]

(17). Foster MW, Mansy SS, Hwang J, Penner-Hahn JE, Surerus KK, Cowan JA. A Mutant Human IscU Protein Contains a Stable $[2Fe2S]^{2+}$ Center of Possible Functional Significance. J. Am. Chem. Soc. 2000; 122:6805–6806.

(18). Agar J, Krebs C, Frazzon J, Huynh BH, Dean DR, Johnson M. IscU as a scaffold for iron-sulfur cluster biosynthesis: sequential assembly of [2Fe-2S] and [4Fe-4S] clusters in IscU. Biochemistry. 2000; 39:7856–7862. [PubMed: 10891064]

(19). Hoff KG, Silberg JJ, Vickery L. Interaction of the iron-sulfur cluster assembly protein IscU with the Hsc66/Hsc20 molecular chaperone system of *Escherichia coli*. Proc. Natl. Acad. Sci. U.S.A. 2000; 97:7790–7795. [PubMed: 10869428]

(20). Uhrigshardt H, Singh A, Kovtunovych G, Ghosh M, Rouault TA. Characterization of the human HSC20, an unusual DnaJ type III protein, involved in iron-sulfur cluster biogenesis. Hum. Mol. Genet. 2010; 19:3816–3834. [PubMed: 20668094]

(21). Füzéry A, Tonelli M, Ta D, Cornilescu G, Vickery L, Markley J. Solution Structure of the Iron-Sulfur Cluster Cochaperone HscB and Its Binding Surface for the Iron-Sulfur Assembly Scaffold Protein IscU. Biochemistry. 2008; 47:9394–9404. [PubMed: 18702525]

(22). Lane DJR, Richardson DR. Frataxin, a molecule of mystery: Trading stability for function in its iron-binding site. Biochem. J. 2010; 426:e1–e3. [PubMed: 20141512]

(23). Yoon T, Cowan J. Iron-sulfur cluster biosynthesis. Characterization of frataxin as an iron donor for assembly of [2Fe-2S] clusters in ISU-type proteins. J. Am. Chem. Soc. 2003; 125:6078–6084. [PubMed: 12785837]

(24). Bulteau A-L, O'Neill HA, Kennedy MC, Ikeda-Saito M, Isaya G, Szweda LI. Frataxin acts as an iron chaperone protein to modulate mitochondrial aconitase activity. Science. 2004; 305:242–245. [PubMed: 15247478]

(25). Adinolfi S, Iannuzzi C, Prischi F, Pastore C, Iametti S, Martin S, Bonomi F, Pastore A. Bacterial frataxin CyaY is the gatekeeper of iron-sulfur cluster formation catalyzed by IscS. Nat. Struct. Mol. Biol. 2009; 16:390–396. [PubMed: 19305405]

(26). Shi R, Proteau A, Villarroya M, Moukadiri I, Zhang L, Trempe J-F, Matte A, Armengod ME, Cygler M. Structural basis for Fe-S cluster assembly and tRNA thiolation mediated by IscS protein-protein interactions. PLoS Biol. 2010; 8:e1000354. [PubMed: 20404999]

(27). Prischi F, Konarev PV, Iannuzzi C, Pastore C, Adinolfi S, Martin SR, Svergun DI, Pastore A. Structural bases for the interaction of frataxin with the central components of iron-sulphur cluster assembly. Nat. Commun. 2010; 1:95. [PubMed: 20981023]

(28). Musco G, Stier G, Kolmerer B, Adinolfi S, Martin SR, Frenkiel TA, Gibson TJ, Pastore A. Towards a structural understanding of Friedreich's ataxia: The solution structure of frataxin. Structure. 2000; 8:695–707. [PubMed: 10903947]

(29). Dhe-Paganon S, Shigeta R, Chi YI, Ristow M, Shoelson SE. Crystal structure of human frataxin. J. Biol. Chem. 2000; 275:30753–30756. [PubMed: 10900192]

(30). Cho S, Lee M, Yang J, Lee J, Song H, Suh S. Crystal structure of *Escherichia coli* CyaY protein reveals a previously unidentified fold for the evolutionarily conserved frataxin family. Proc. Natl. Acad. Sci. U.S.A. 2000; 97:8932–8937. [PubMed: 10908679]

(31). Cook JD, Kondapalli KC, Rawat S, Childs WC, Murugesan Y, Dancis A, Stemmler TL. Molecular details of the yeast frataxin-Isu1 interaction during mitochondrial Fe-S cluster assembly. Biochemistry. 2010; 49:8756–8765. [PubMed: 20815377]

(32). Leidgens S, De Smet S, Foury F. Frataxin interacts with Isu1 through a conserved tryptophan in its β-sheet. Hum. Mol. Genet. 2010; 19:276–286. [PubMed: 19884169]

(33). Wang T, Craig EA. Binding of yeast frataxin to the scaffold for Fe-S cluster biogenesis, Isu. J. Biol. Chem. 2008; 283:12674–12679. [PubMed: 18319250]

(34). Shan Y, Napoli E, Cortopassi GA. Mitochondrial frataxin interacts with ISD11 of the NFS1/ISCU complex and multiple mitochondrial chaperones. Hum. Mol. Genet. 2007; 16:929–941. [PubMed: 17331979]

(35). Tsai CL, Bridwell-Rabb J, Barondeau DP. Friedreich's ataxia variants I154F and W155R diminish frataxin-based activation of the iron-sulfur cluster assembly complex. Biochemistry. 2011; 50:6478–6487. [PubMed: 21671584]

(36). Gill SC, von Hippel PH. Calculation of protein extinction coefficients from amino acid sequence data. Anal. Biochem. 1989; 182:319–326. [PubMed: 2610349]

(37). Marelja Z, Stöcklein W, Nimtz M, Leimkühler S. A novel role for human Nfs1 in the cytoplasm: Nfs1 acts as a sulfur donor for MOCS3, a protein involved in molybdenum cofactor biosynthesis. J. Biol. Chem. 2008; 283:25178–25185. [PubMed: 18650437]

(38). Siegel LM. A direct microdetermination for sulfide. Anal. Biochem. 1965; 11:126–132. [PubMed: 14328633]

(39). Huang J, Cowan JA. Iron-sulfur cluster biosynthesis: Role of a semi-conserved histidine. Chem. Commun. 2009; 21:3071–3073.

(40). Di Cera E. Kinetics of Allosteric Activation. Methods Enzymol. 2009; 466:259–271. [PubMed: 21609865]

(41). Leslie AGW. Recent changes to the MOSFLM package for processing film and image plate data. Joint CCP4+ESF– EAMCB Newsletter on Protein Crystallography. 1992; (No. 26)

(42). Collaborative Computational Project Number 4. The CCP4 suite: Programs for protein crystallography. Acta Crystallogr. 1994; D50:760–763.

(43). McCoy AJ, Grosse-Kunstleve RW, Adams PD, Winn MD, Storoni LC, Read RJ. Phaser crystallographic software. J. Appl. Crystallogr. 2007; 40:658–674. [PubMed: 19461840]

(44). McRee DE. XtalView/Xfit: A Versatile Program for Manipulating Atomic Coordinates and Electron Density. J. Struct. Biol. 1999; 125:156–165. [PubMed: 10222271]

(45). Winn MD, Murshudov GN, Papiz MZ. Macromolecular TLS refinement in REFMAC at moderate resolutions. Methods Enzymol. 2003; 374:300–321. [PubMed: 14696379]

(46). Brunger AT. The Free R value: A Novel Statistical Quantity for Assessing the Accuracy of Crystal Structures. Nature. 1992; 355:472–474. [PubMed: 18481394]

(47). Yoon T, Dizin E, Cowan JA. N-terminal iron-mediated self-cleavage of human frataxin: Regulation of iron binding and complex formation with target proteins. J. Biol. Inorg. Chem. 2007; 12:535–542. [PubMed: 17285345]

(48). Tanaka F, Fuller R, Shim H, Lerner RA, Barbas CF III. Evolution of aldolase antibodies in vitro: Correlation of catalytic activity and reaction-based selection. J. Mol. Biol. 2004; 335:1007–1018. [PubMed: 14698295]

(49). Gong XM, Paddock ML, Okamura MY. Interactions between cytochrome c2 and photosynthetic reaction center from *Rhodobacter sphaeroides*: Changes in binding affinity and electron transfer rate due to mutation of interfacial hydrophobic residues are strongly correlated. Biochemistry. 2003; 42:14492–14500. [PubMed: 14661961]

(50). Schwarz A, Pierfederici FM, Nidetzky B. Catalytic mechanism of α-retaining glucosyl transfer by *Corynebacterium callunae* starch phosphorylase: The role of histidine-334 examined through kinetic characterization of site-directed mutants. Biochem. J. 2005; 387:437–445. [PubMed: 15535798]

(51). Campuzano V, Montermini L, Lutz Y, Cova L, Hindelang C, Jiralerspong S, Trottier Y, Kish SJ, Faucheux B, Trouillas P, Authier F. o. Dürr A, Mandel JL, Vescovi A, Pandolfo M, Koenig M. Frataxin is reduced in Friedreich ataxia patients and is associated with mitochondrial membranes. Hum. Mol. Genet. 1997; 6:1771–1780. [PubMed: 9302253]

(52). Willis J, Isaya G, Gakh O, Capaldi R, Marusich M. Lateral-flow immunoassay for the frataxin protein in Friedreich's ataxia patients and carriers. Mol. Genet. Metab. 2008; 94:491–497. [PubMed: 18485778]

(53). Deutsch EC, Santani AB, Perlman SL, Farmer JM, Stolle CA, Marusich MF, Lynch DR. A rapid, noninvasive immunoassay for frataxin: Utility in assessment of Friedreich ataxia. Mol. Genet. Metab. 2010; 101:238–245. [PubMed: 20675166]

(54). Steinkellner H, Scheiber-Mojdehkar B, Goldenberg H, Sturm B. A high throughput electrochemiluminescence assay for the quantification of frataxin protein levels. Anal. Chim. Acta. 2010; 659:129–132. [PubMed: 20103114]

(55). Saccà F, Puorro G, Antenora A, Marsili A, Denaro A, Piro R, Sorrentino P, Pane C, Tessa A, Morra V. Brescia, Cocozza S, De Michele G, Santorelli FM, Filla A. A combined nucleic acid and protein analysis in friedreich ataxia: Implications for diagnosis, pathogenesis and clinical trial design. PLoS One. 2011; 6:e17627. [PubMed: 21412413]

Figure 1.
Native frataxin structure and overlay with W155R, W155A, and W155F variants. (A) Overall structural fold of FXN with surface-exposed residues. (B) Overlay of native FXN (green), W155R (magenta), W155A (cyan), and W155F (yellow) structures.
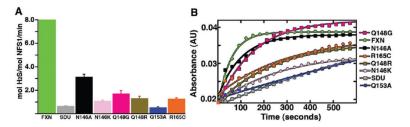
Figure 2.
Frataxin variants are less able to activate cysteine desulfurase activity and Fe–S cluster biosynthesis. (A) Sulfide production was assessed in the presence of 1 equiv of the NFS1–ISD11 complex, 3 equiv of each FXN variant, 3 equiv of ISCU2, and 10 equiv of ferrous iron. Error bars are for three independent measurements. (B) Fe–S cluster formation was monitored by an increase in absorbance at 456 nm as a function of time. Assays included the NFS1–ISD11 complex with 3 equiv of ISCU2 and 3 equiv of FXN variants. The lines through the data are the fits using first-order kinetics.
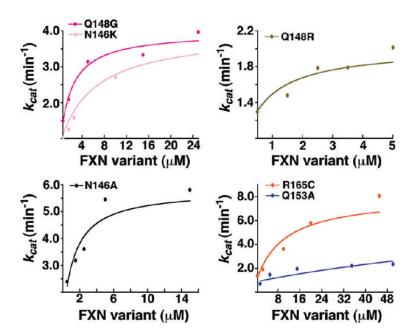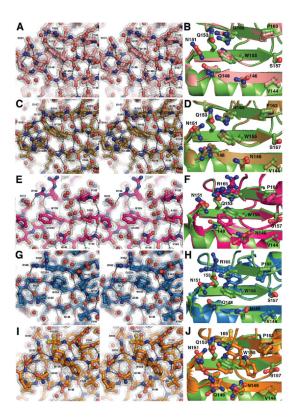
Figure 3.
Determination of binding constants for FXN variants. k_{cat} was determined at different FXN concentrations. The lines through the data are the fits as a type II allosteric activator to eq 1. The R^2 values are 0.920, 0.965, 0.856, 0.886, 0.867, and 0.915 for the N146K, Q148G, Q148R, N146A, Q153A, and R165C variants, respectively.

Figure 4.
Crystal structures of the N146K, Q148R, Q148G, Q153A, and R165C variants. Stereo images with $2F_o - F_c$ electron density contoured at 1σ for (A) N146K, (C) Q148R, (E) Q148G, G (Q153A), and (I) R165C structures. Panels B, D, H show overlays of N146K (salmon), Q148R (sand), and Q153A (blue) with native FXN (green), respectively. Panels F and J show overlays of the four independent molecules of Q148G (hot pink) and two independent molecules of R165C (orange) overlaid with native FXN (green), respectively.
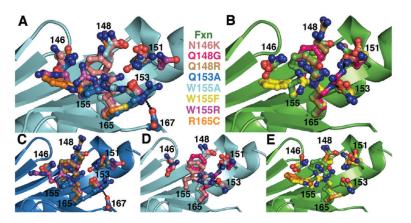
Figure 5.
Grouping of FXN variant structures by their ability to bind and activate the SDU complex. Structural overlay for (A) class I (Q153A and W155R) and II (R165C, N146K, and W155A) variants that bind the SDU complex at least 25-fold more weakly than FXN, (B) class III (Q148R) and IV (W155F and Q148G) variants that bind the SDU complex 3–10-fold more weakly than FXN, (C) class I (Q153A and W155R) and class III (Q148R) variants that have k_{cat} values that are <30% of that of FXN, (D) class II (N146K and W155A) and IV (Q148G) variants that have k_{cat} values that are between 45 and 50% of that of FXN, and (E) class II (R165C) and IV (W155F) variants that exhibit k_{cat} values that are >50% of that of FXN. The color scheme is as follows: green for FXN, salmon for N146K, hot pink for Q148G, sand for Q148R, sky blue for Q153A, cyan for W155A, yellow for W155F, magenta for W155R, and orange for R165C.
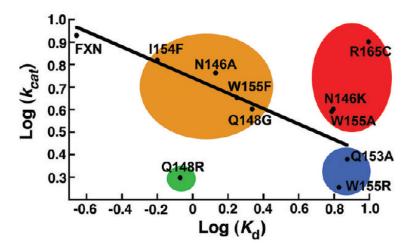
Figure 6.
Correlation between the binding constant and the k_{cat} of the cysteine desulfurase reaction for the SDUF complex with different FXN variants. The different classes of variants are highlighted in blue (class I), red (class II), green (class III), and orange (class IV).

Table 1

Summary of Activity, Binding, and Kinetic Parameters for FXN Variants

complex	FXN class[a]	NFS1 activity (units/min)	Fe–S cluster formation (units/min)	FXN K_d (μM)	k_{cat} (min^{-1})	K_M^{Cys} (mM)	k_{cat}/K_M (M^{-1} s^{-1})
SDU–FXN[b]		8.25 ± 0.90	12.3 ± 0.4	0.22 ± 0.05	8.5 ± 0.3	0.014 ± 0.002	9800 ± 1700
SDU–N146A	IV	3.13 ± 0.24	10.1 ± 1.1	1.35 ± 0.25	5.8 ± 0.2	0.021 ± 0.004	4700 ± 1000
SDU–N146K	II	1.08 ± 0.08	2.8 ± 0.3	6.25 ± 1.40	4.0 ± 0.1	0.019 ± 0.004	3500 ± 700
SDU–Q148G	IV	1.71 ± 0.27	4.7 ± 0.1	2.17 ± 0.28	4.0 ± 0.1	0.009 ± 0.002	7000 ± 1600
SDU–Q148R	III	1.29 ± 0.20	2.9 ± 0.2	0.85 ± 0.15	2.0 ± 0.1	0.019 ± 0.004	1800 ± 300
SDU–Q153A	I	0.52 ± 0.08	0.8 ± 0.2	7.50 ± 2.18	2.4 ± 0.1	0.014 ± 0.003	2900 ± 600
SDU–R165C	II	1.26 ± 0.10	4.1 ± 0.9	10.40 ± 2.26	8.1 ± 0.1	0.012 ± 0.001	11000 ± 1400
SDU–I154F[c]	IV	4.14 ± 0.20	7.6 ± 0.5	0.63 ± 0.14	6.6 ± 0.4	0.025 ± 0.004	4400 ± 800
SDU–W155R[c]	I	0.60 ± 0.07	0.9 ± 0.1	6.73 ± 1.28	1.8 ± 0.1	0.013 ± 0.003	2300 ± 500
SDU–W155A[c]	II	0.83 ± 0.28	2.0 ± 0.1	6.12 ± 1.36	3.9 ± 0.2	0.012 ± 0.003	5600 ± 1600
SDU–W155F[c]	IV	2.09 ± 0.51	3.4 ± 0.1	1.78 ± 0.31	4.5 ± 0.1	0.018 ± 0.003	4100 ± 800
SDU[b]		0.65 ± 0.02	0.7 ± 0.1	not available	0.89 ± 0.04	0.59 ± 0.05	25 ± 3

[a]FXN classes are defined in the Discussion.

[b]See ref 11.

[c]See ref 35.

Table 2

X-ray Data Collection and Refinement Statistics

	N146K	Q148G	Q148R	Q153A	R165C
Data Collection					
beamline	APS 23-ID-D	SSRL BL11-1	SSRL BL7-1	SSRL BL7-1	ALS BL4-2-2
wavelength (Å)	1.0331	1.0971	0.9794	0.9794	1.0000
space group	$P2_1$	$P1$	$P2_12_12_1$	$C2$	$C2$
unit cell dimensions	$a = 30.47$ Å, $b = 45.82$ Å, $c = 38.9$ Å, $\beta = 97.36°$	$a = 46.41$ Å, $b = 68.56$ Å, $c = 89.97$ Å, $\beta = 93.23°$	$a = 42.53$ Å, $b = 45.31$ Å, $c = 69.12$ Å, $\beta = 91.87°$	$a = 87.44$ Å, $b = 32.46$ Å	$a = 86.02$ Å, $b = 32.12$ Å, $c = 92.08$ Å, $\beta = 90.16°$
no. of molecules per asymmetric unit	1	4	1	1	2
resolution (Å)	30.33–1.70	26.19–1.38	28.29–1.24	25.37–1.15	19.5–1.57
outer shell (Å)	1.79–1.70	1.45–1.38	1.31–1.24	1.21–1.15	4.96–1.57
no. of observations	84900	787564	517442	318181	128770
no. of unique observations	11654	111516	38275	45196	35106
redundancy	7.3	7.1	13.5	7.0	3.7
completeness (%)[a]	98.9 (100)	96.7 (94.7)	99.6 (99.2)	99.4 (99.7)	98.8 (98.0)
mean $I/(\sigma I)$[a]	20.2 (10.1)	14.5 (2.3)	27.2 (9.4)	19.0 (4.5)	11.5 (4.3)
R_{sym} (%)[a,b]	5.9 (13.9)	7.0 (84.7)	5.6 (28.5)	6.0 (40.1)	6.2 (33.1)
Refinement					
residues not in model	82–85	82–88	82–88	82–89	82–89
solvent atoms	66	352	127	95	133
R_{work}/R_{free} (%)[c]	21.4/24.5	19.9/22.7	18.3/19.7	16.7/17.9	21.6/25.2
rmsd for bond lengths (Å)	0.008	0.032	0.030	0.030	0.025
rmsd for bond angles (deg)	1.2	2.5	2.2	2.4	2.3
Ramachandran (%)					
most favored	96.2	94.7	95.3	94.3	92.0
additional allowed	3.8	5.3	4.7	5.7	8.0

	N146K	Q148G	Q148R	Q153A	R165C
generous	0	0	0	0	0
disallowed	0	0	0	0	0
PDB entry	3T3J	3T3T	3T3K	3T3L	3T3X

[a] Values in parentheses are the statistics for the highest-resolution shell of data.

[b] $R_{sym} = S|I_{hkl} - \langle I \rangle|/S\langle I \rangle$, where $\langle I \rangle$ is the average individual measurement of I_{hkl}.

[c] $R_{work} = (S|F_{obs} - F_{calc}|)/S|F_{obs}|$, where F_{obs} and F_{calc} are the observed and calculated structure factors, respectively. R_{free} is calculated in the same manner as R_{work}, but from the data (5%) that were excluded from the refinement.